Catalysis Today 177 (2011) 12–24

Contents lists available at ScienceDirect

Catalysis Today

journal homepage: www.elsevier.com/locate/cattod

Experimental and theoretical IR study of methanol and ethanol conversion over H-SAPO-34

Karen Hemelsoet[a,b,*], An Ghysels[a,1], Davide Mores[b], Kristof De Wispelaere[a], Veronique Van Speybroeck[a], Bert M. Weckhuysen[b], Michel Waroquier[a,**]

[a] Center for Molecular Modeling (CMM), Ghent University, Technologiepark 903, B-9052 Zwijnaarde, and QCMM-Alliance, Ghent-Brussels, Belgium
[b] Inorganic Chemistry and Catalysis, Debye Institute for Nanomaterials Science, Utrecht University, Universiteitsweg 99, Utrecht, The Netherlands

ARTICLE INFO

Article history:
Received 11 February 2011
Received in revised form 23 May 2011
Accepted 30 May 2011
Available online 23 July 2011

Keywords:
Methanol to hydrocarbons
IR
H-SAPO-34
DFT calculations
In situ DRIFT measurements
Normal mode analysis

ABSTRACT

Theoretical and experimental IR data are combined to gain insight into the methanol and ethanol conversion over an acidic H-SAPO-34 catalyst. The theoretical simulations use a large finite cluster and the initial physisorption energy of both alcohols is calculated. Dispersive contributions turn out to be vital and ethanol adsorbs stronger than methanol with approximately 14 kJ mol^{-1}. Calculated IR spectra of the alcohols and of formed aromatic cations upon conversion are also analyzed and support the peak assignment of the experimental in situ DRIFT spectra, in particular for the C–H and C= C regions. Theoretical IR spectra of the gas phase compounds are compared with those of the molecules loaded in a SAPO cluster and the observed shifts of the peak positions are discussed. To get a better understanding of these framework–guest interactions, a new theoretical procedure is proposed based on a normal mode analysis. A cumulative overlap function is defined and enables the characterization of individual peaks as well as induced frequency shifts upon adsorption.

1. Introduction

The characterization of reaction intermediates of complex catalytic processes can occur via a variety of spectroscopic techniques; it nevertheless always remains an extremely challenging task from a purely experimental viewpoint. Nowadays, theoretical simulations of realistic model systems are feasible and they can hence supply valuable complementary information. A combination of experiment and theory already provided insight into the reaction mechanism of several commercially important catalytic processes, including the intensively explored methanol to hydrocarbons process. This conversion of methanol or another methylating agent occurs over microporous solid acids such as zeolites and zeotypes [1,2] and H-ZSM-5 and H-SAPO-34 are at present the most important industrially applied materials. The actual reaction mechanism is particularly complex and consists of many parallel routes. There is now general consensus about the hydrocarbon pool (HP) mechanism assuming that organic reaction centres act as co-catalysts inside the zeolite pores [2–6]. The HP intermediates serve as platforms to which C_1 species can add and from which primary olefin products can dissociate. The actual active catalyst is thus the combined organic–inorganic supramolecular complex of the HP and zeolite framework. Many studies focussed on olefin eliminating cycles in H-ZSM-5 for which dual aromatic and alkene based routes are both shown to be active [7–12]. If not limited by space restrictions, as is the case in H-SAPO-34 or H-Beta, the aromatic HP species are known to be the higher methylated benzene derivatives [13–15]. Recently Wang et al. claimed on basis of periodic DFT calculations in H-SAPO-34 that methylbenzenes (MBs) with five or six methyl groups are not more reactive than those with fewer methyl groups [16,17]. In addition to the methylbenzenes, methylnaphthalenes were also found to be active HP species exhibiting a high initial selectivity for ethylene [18]. Recent theoretical calculations indicated that exocyclic methylation of these bulky compounds exhibits a very high activation barrier (175.7 kJ mol^{-1} at 670 K) and hence a low reaction rate [19]. Concluding there is still a lot of discussion on the particular nature of the HP species. Recently experimental evidence was given that depending on the material's topology other hydrocarbons play an active role in the reaction mechanism [8,20,21]. In addition to methanol conversion, ethanol has gained attention as possible feedstock. Madeira et al. studied ethanol conversion over three different zeolites (H-FAU, H-Beta, H-MFI) and a high activity for C_{3+} hydrocarbon production was

* Corresponding author at: Center for Molecular Modeling (CMM), Ghent University, Technologiepark 903, Belgium. Fax: +32 9 264 65 60.
** Corresponding author. Fax: +32 9 264 65 60.
E-mail addresses: Karen.Hemelsoet@UGent.be (K. Hemelsoet), Michel.Waroquier@UGent.be (M. Waroquier).
[1] Current address: Department of Chemistry, University of California – Berkeley, Gilman Hall, 94720 Berkeley, CA, USA.

0920-5861/$ – see front matter © 2010 Elsevier B.V. All rights reserved.
doi:10.1016/j.cattod.2011.05.040

observed [22,23]. Little is known about the ethanol conversion over H-SAPO-34, although Dahl et al. pointed out that ethanol rapidly dehydrates to ethene, which only reacted over H-SAPO-34 after activation with a propene pulse [24].

In H-SAPO-34, the aromatic HP species can readily age into larger aromatic compounds which block the active sites and severely restrict mass transport [15,25,26]. Haw and Marcus outlined possible aging routes that lead to less active, aromatic species which are entrapped in the zeolitic pore and will remain there until regeneration of the catalyst [15]. Thus far, no exact mechanisms for the growth of these large (methylated) polyaromatics are known; a problem which is enforced by the generally poor characterization of large carbonaceous compounds. The nature of the coke species in H-ZSM-5 and H-SAPO-34 has been studied by Mores et al. using in situ UV/VIS spectroscopy combined with confocal fluorescence micro-spectroscopy. Graphitic coke on H-ZSM-5 crystals is initially formed at the edges of the crystal, whereas in H-SAPO-34 aromatic coke compounds are mainly formed inside the crystals [27]. The same experimental approach was used for analyzing a set of individual H-ZSM-5 crystals with different Brønsted acidity (Si/Al ratio ranging between 11 and 44), and indicated that an increased acid site density facilitates the formation of larger coke species and enhances their formation rate [28]. In situ Raman data of Wragg et al. also point out the formation of larger aromatic compounds inside H-SAPO-34, inducing strain in the zeolitic lattice [29]. IR spectroscopy provides another technique and is extensively used to study interactions between basic molecules and the zeolitic Brønsted acid site since the formation of medium-strong hydrogen bonds has peculiar infrared features [30–32]. A recent review of Lamberti et al. discusses the use of in situ IR spectroscopy for probing the surfaces of heterogeneous catalysts using H_2, CO, NO and C_2H_4[33]. Experimental FTIR studies of H-SAPO-34 catalysts were performed by Marchese et al., investigating host–guest and guest–guest interactions of morpholine in H-SAPO-34 [34]. Calculated vibrational modes were consequently used to assign the main absorptions of morpholinium and indicated the importance of additional water molecules [35]. A study on the adsorption of methanol and water in H-SSZ-13 and H-SAPO-34 indicated that protonated species can be formed in the former material, whereas the smaller acidity of the aluminophosphate only leads to hydrogen bonded species in H-SAPO-34 [36]. Palumbo et al. used IR in combination with UV/VIS to study the formation of carbonaceous compounds in H-ZSM-5 and methylated aromatic carbocationic species were found to be present as coke precursors [37]. The topology specific structure–activity relationship was investigated by in situ IR for the MTO reaction comparing six zeolites (CHA, LTA, MFI, BEA, MOR and FAU) [38]. It was found that the concentration of methylbenzenes principally depends on the number of strong acid sites, whereas the deactivation rate is dominated by the pore topology.

FTIR of probe molecules combined with MAS NMR spectroscopy proved to be another valuable tool which has in particular been used to describe the silicon distribution and site location of hydroxyls in SAPO materials. For a review on this topic, we refer to Pastore et al. [39]. Generally speaking, three possible mechanisms allow for insertion of Si in aluminophosphates. Replacement of an aluminum atom by a silicon (SM1), replacement of a phosphorous atom by silicon and a proton (SM2) or the double substitution of neighboring Al and P by two Si atoms (SM3). Since Si–O–P bonds are unlikely [40–43], only the SM2 or a combined SM2 + SM3 mechanism have found experimental evidence. The combined mechanism leads to the formation of silicate islands which have been shown to possess strong acid sites at their borders [44,45]. The relative importance of the different substitution mechanisms depends on the complex interplay of various factors, such as template and synthesis conditions [39,46]. Using tetraethylammonium hydroxide as a template, the chabazite cage can host only one template molecule leading to a material with only one acid site per cage whereas a material with two acid sites per cage can be synthesized using morpholine as a template [15,46]. In the case of H-SAPO-34, Barthomeuf has shown based on topological grounds that above $x_{Si} \approx 0.11$ the SiO_4 tetrahedra cannot be isolated, meaning that silicate aggregates will be present in the sample [47]. Their presence is evident from ^{29}Si MAS NMR data, revealing peaks in the range −93 to −115 ppm whereas an isolated Si atom (indicated as Si(4Al) species) reveals a distinct peak at −90 ppm [39,46,48]. The stability of clusters comprising Si–O–Si bridges was confirmed using theoretical simulations by Sastre et al. [49], who also reported deprotonation energies and OH stretching frequencies of the various acid sites [45].

Molecular simulations on extended zeolitic systems have become a ubiquitous tool as it allows to study in detail single reaction steps of complex reaction networks. The nanoporous topology can be taken into account by periodic calculations in which one or more unit cells of the zeolite are considered or by a finite cluster, provided it is large enough to include a large portion of the material. Two recent computational studies investigated in detail methylation reactions on alkenes within an acidic H-ZSM-5 catalyst. It was shown that both enthalpy barriers [50] and rate coefficients [51] of individual reactions can now be calculated with “near chemical accuracy”. In the latter work, large finite clusters and a hybrid QM/MM ONIOM calculation scheme were applied. The large finite clusters were saturated with fixed outer hydrogens and a normal mode analysis was hence performed using the partial Hessian vibrational analysis (PHVA) method [52–56]. In addition to the PHVA scheme, other vibrational analysis schemes can be applied to study extended systems. In particular, the Mobile Block Hessian (MBH) method [56–59] introduces rigid regions in the system (blocks) as a result of which internal vibrations are kept fixed. This concept can serve as a tool to identify vibrational modes in the spectrum and to filter the spectrum in order to focus on a particular region. This is the approach followed in this work: a combined PHVA–MBH approach is employed to identify the normal modes of the guest species in the spectrum of a framework–guest complex. Along the same line, also the framework vibrations can be separated from the full spectrum allowing to study the shift induced by adsorption of various guest molecules. Very recently both the PHVA and MBH methods were tested by De Moor et al. to calculate the adsorption entropies of n-octane and isobutene in H-ZSM-22 and H-FAU using periodic DFT simulations [60]. They showed that the computationally less demanding PHVA scheme leads to calculated physisorption and chemisorption entropies which are in good agreement (maximal deviation of 10 J mol^{-1} K^{-1}) with those obtained from a full hessian calculation, provided stricter convergence criteria are used for the optimization. For loosely bonded complexes the mobile block adsorbate method was applied leading to predicted physisorption entropies within an accuracy of 10–15 J mol^{-1} K^{-1} compared to the experimental values. Both methods lead to a considerable reduction of the computational cost.

In this work, the adsorption of methanol and ethanol in a large finite silico-alumino-phosphate cluster is examined from first principle calculations. The corresponding computed IR spectra are discussed next. Furthermore, calculated IR spectra of singly methylated aromatic cations both in gas phase and in the zeolitic environment are given. These species are likely to be formed in the zeolitic pore during methanol and ethanol conversion and represent hydrocarbon pool (HP) and coke-like species. The theoretical data are matched with experimental in situ DRIFT spectra and lead to identification of various bands. In a final section an analysis procedure is presented using different NMA schemes (PHVA and PHVA–MBH) which will aid to unravel the complex vibrational spectra and thus enable a more systematic assignment of the observed peaks. It is our aim to show how the combined PHVA–MBH approach is a powerful tool for scanning and inter-

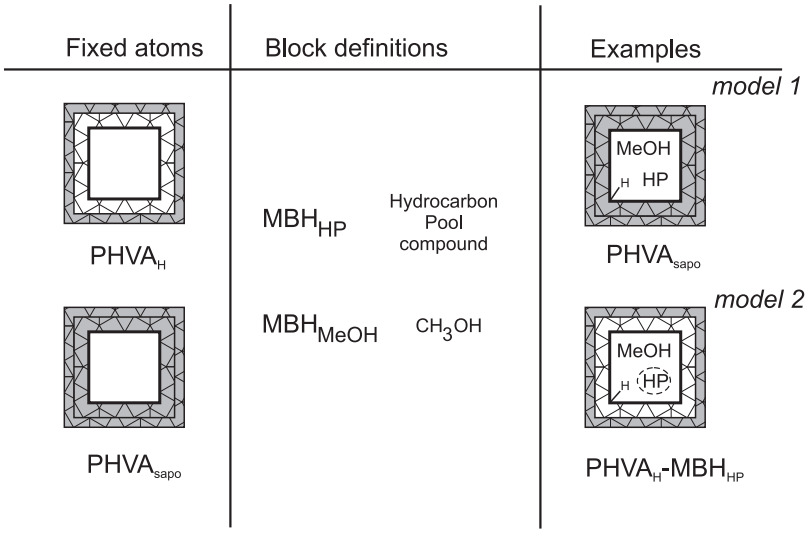

Fig. 1. Representation of the investigated NMA schemes. The fixed atoms in the PHVA schemes are the saturating hydrogens (PHVA$_H$) or the SAPO atoms (PHVA$_{sapo}$). The PHVA can be combined with any MBH block choice. In the right column some examples studied in this work are depicted representing a SAPO cluster loaded with methanol and a HP compound. In model 1 all atoms belonging to the SAPO framework are constrained during the NMA, whereas the methanol and HP are unconstrained. In model 2 the outer hydrogen atoms are constrained and the internal structure of the HP species is kept fixed (indicated by a dashed frame), the methanol molecule is entirely unconstrained during the NMA. The acid proton is visualized here to illustrate it is unconstrained; however in the remainder of the figures it will be omitted.

preting theoretical spectra and hence support the interpretation of experimental spectra.

2. Computational and experimental details

2.1. Theoretical simulations

2.1.1. Catalyst model and level of theory

The investigated silico-aluminophosphate has the chabazite (CHA) topology which is characterized by spacious cages interconnected by small windows. In this work all calculations were performed on a 44T finite zeolite cluster cut out of the CHA crystallographic structure and one acid site per cage is simulated. This acid site originates from the insertion of a Si at a phosphorous site, inducing a negative framework charge which is counterbalanced by a proton forming a Si–OH–Al bridge (SM2 mechanism). The outer hydrogen atoms of the cluster were constrained in space to prevent unphysical deformations due to the neglect of the full molecular environment. Structures for starting geometries were build using the in-house developed software package Zeobuilder [61,62]. The computations are performed with the Gaussian03 package [63] using a well-established multi-layered method combining an ONIOM(B3LYP/dgtzvp:HF/dgtzvp) energy and ONIOM(B3LYP/dgtzvp:MNDO) geometry. The high level is composed of a 6T cluster which is constructed spatially symmetric around the active site. The true nature of the stationary points was confirmed by a normal mode analysis at the level of theory of the geometry optimization, resulting in only positive frequencies for all minima. Van der Waals contributions are taken into account by using the DFT-D approach as implemented in the Orca software package [64]. Using the optimized ONIOM(B3LYP/dgtzvp:MNDO) geometries, the B3LYP-D method was used to quantify the order of magnitude of the dispersion interactions. In this scheme, the dispersive energy is described by damped interatomic potentials of the form C_6R^{-6} [65]. Analysis of IR spectra has been performed using the GaussView visualization software [66], the spectra are plotted in the range 4000–0 cm^{-1} using a full width at half maximum (FWHM) of 4 cm^{-1}. Computed harmonic vibrational frequencies are typically larger than the experimentally observed fundamentals, due to the neglect of anharmonic effects, the incomplete incorporation of electron correlation and the use of a finite basis set. Using the acidic O–H absorption peak of the fresh H-SAPO-34 material as a benchmark, a scale factor of 0.9641 was obtained, which is in line with reported scale factors for the B3LYP functional combined with a basis set of triple-zeta quality [67].

2.1.2. Detailed normal mode analysis: PHVA and PHVA–MBH

A normal mode analysis (NMA) of a system consists of diagonalizing the (mass-weighted) Hessian, which is the matrix containing the second derivatives of the energy with respect to the atom positions. The resulting eigenvalues and eigenvectors are the frequencies and vibrational modes respectively. In the case of periodic calculations, a full Hessian vibrational analysis (FHVA) is possible, however this is computationally very demanding. In the studied 44T clusters, the saturating hydrogen atoms are constrained during the geometry optimization to prevent the unphysical collapse of the finite cluster. Such a partial geometry optimization with fixed hydrogens asks for an adapted NMA method: the saturating hydrogens should also be kept fixed during the vibrational analysis to ensure consistency. This is accomplished by the partial Hessian vibrational analysis (PHVA), where first the rows and columns corresponding to the fixed atoms are deleted from the Hessian and then this smaller submatrix is diagonalized [52–56]. This NMA scheme is labeled as PHVA$_H$, referring to the hydrogens as the fixed atoms. The PHVA model has previously successfully been applied in MFI- and CHA-type catalysts leading to thermodynamic and kinetic results of relevant individual reaction steps [10,51,60,68,69].

Fixing the hydrogens is indispensable to allow a proper geometry optimization but more atoms can be fixed during the vibrational analysis although they have never been constrained during the optimization process. Fig. 1 schematically presents the two choices of the fixed region considered in this paper: (1) all saturating hydrogens in the minimal scheme PHVA$_H$; (2) all SAPO-atoms, including the saturating hydrogens, in the scheme PHVA$_{sapo}$. The second choice, PHVA$_{sapo}$, is motivated by the fact that it allows to filter out the framework frequencies from the complex spectra. In both schemes, the acid proton is unconstrained.

A combined PHVA–MBH model was applied to further analyze the spectra. In the Mobile Block Hessian method, groups of atoms are considered as mobile blocks during the vibrational analysis

[56,57]. Individual atom motions are not allowed in the block, but the block as a whole can translate and rotate as a rigid unit. As such, the internal vibrations within each block will be absent from the spectrum and thus this method allows to filter some of the internal motions from the full vibrational spectrum. In this paper, particular block choices are considered, as indicated in Fig. 1. For e.g., the scheme $PHVA_H$–MBH_{HP} (model 2 in Fig. 1), applied on the SAPO cluster loaded with methanol and a hydrocarbon pool (HP) species, filters out the frequencies of the hydrocarbon from the full spectrum. The lower the coupling between the framework and the motions of the guest molecules, the better the filtering performs.

In addition, a cumulative overlap analysis of the normal modes calculated in various schemes allows to provide further insight in the frequencies associated with adsorption of a guest species in the SAPO cluster. The overlap between two modes i and j calculated according to two methods (e.g. models 1 and 2 of Fig. 1) is defined as the square of the dot product between the mass-weighted and normalized mode vectors v_i^1 and v_j^2. This number between 0 and 1 thus expresses the similarity between the two modes. The cumulative overlap of a mode i calculated with model 1 versus model 2 is defined as [59,70]

$$O_i = \sum_j |v_i^1 \cdot v_j^2|^2 \quad (1)$$

The cumulative overlap O_i expresses to what extent a mode i calculated with model 1 is still present in the spectrum when using model 2. A value close to 0% indicates that the mode i is nearly completely filtered out, whilst a value close to 100% means that mode i is also reproduced when applying model 2. Hence the cumulative overlap can serve as a technique to identify the character of the modes by comparing different PHVA and PHVA–MBH schemes. A second application of the cumulative overlap is the visualization of the induced shifts caused by framework–guest interactions, i.e. the shifts in the spectrum when a compound is brought inside a zeolitic framework. First, the reference spectrum is the full spectrum of the compound in gas phase, calculated with the standard NMA method (without fixed atoms). Next, the cumulative overlap is used to identify the frequencies of the compound adsorbed in the framework, as described above. Finally by superimposing the gas phase spectrum and the cumulative overlap, the shift of the peak locations induced by adsorption of the guest molecule can be visualized.

The aim of this detailed NMA analysis (see Section 3.3) is to unravel the separate contributions of the zeolitic framework and the various guest molecules in the calculated vibrational spectra. These are plotted as a density of states (d.o.s.) spectrum [71] where each Gaussian shaped peak has an equal amplitude (IR intensity is not taken into account) using a FWHM of 10 cm^{-1}. This post-processing analysis been done using the in-house developed software TAMkin, a free and versatile toolkit for NMA and chemical kinetics [72].

2.2. In situ IR experiments

In situ Diffuse Reflectance Infrared Fourier Transform (DRIFT) Spectroscopy measurements were performed on a Bruker Tensor 27 instrument utilizing a HVC-DRP-3 Diffuse Reflectance Reaction Chamber containing CaF_2 windows and a MCT detector. The bottom of the sample cup was filled with siliconcarbide in order to restrict thermal gradients and a grid separated the sample from the SiC. Freshly calcined SAPO-34 (1.0–2.0 μm with a (Al + P)/Si ratio of 7, obtained through SEM-EDX measurements) was heated at 300 °C for 3 h under inert atmosphere. The amount of Si (x_{Si} = 0.12) suggests the presence of silicate islands in our sample. This was indeed confirmed by means of ^{29}Si NMR data, showing signals in the range −90 to −120 ppm (pointing at Si(nAl) species with n < 4) in addition to the clear peak around −90 ppm (characteristic of Si(4Al) species). For a detailed characterization of the catalytic sample we refer to Ref. [73]. Consecutive pulses of 5 × 5 s, 5 × 15 s and 40 × 30 s with 50 ml/min introduced the reactant in the sample. The spectra were recorded every 2 min from 4000 to 1000 cm^{-1} with 50 scans accumulation and 4 cm^{-1} resolution.

3. Results and discussion

Section 3.1 presents the theoretical results of the physisorption of methanol and ethanol in H-SAPO-34. Corresponding calculated IR spectra of these alcohols and some hydrocarbons formed after alcohol conversion in the SAPO cluster as well as experimental DRIFT spectra are given in Section 3.2. The analysis procedure based on NMA and the cumulative overlap is explained and illustrated using three case studies in Section 3.3; the vibrational spectra of (i) a SAPO framework loaded with methanol, (ii) a framework loaded with naphthalene and (iii) an empty cluster are discussed.

3.1. Physisorption of methanol and ethanol in H-SAPO-34 from first principle calculations

The exact nature of adsorbed alcohol complexes has received a lot of attention in literature [74–84]. Mainly the issue whether the adsorbed complex is a neutral hydrogen-bonded (physisorbed) or a positively charged protonated (chemisorbed) complex is heavily debated. The nature of the alcohol, the acidity and topology of the zeolite framework and the coverages of the guest molecules determine the final outcome [84–86]. Also for the CHA topology, a broad set of theoretical calculations were performed but they initially did not uniquely determine the answer as the final outcome is largely dependent on the particular theoretical protocol that was used for the calculations (periodic versus cluster calculations, size of the cluster) [84–90]. Small cluster calculations lead to the observation that methanol was physisorbed on the acid site, whereas Shah et al. used periodic DFT calculations to reveal that the optimized geometry of adsorbed methanol in CHA corresponds to the methoxonium ion (i.e. chemisorption of methanol). Later Haase et al. [91] showed by periodic molecular dynamics calculations that two minima exist: the hydrogen-bonded physisorbed complex and the protonated chemisorbed complexes. This was later confirmed by Stich et al. [92] and Mihaleva et al. [93], who also predicted that B3LYP geometries were fairly accurate based on the comparison of calculated methanol hydroxyl frequencies with experimental ones. A comprehensive overview of calculated adsorption energies of methanol in CHA can be found in Ref. [94]. The silico-aluminophosphate (SAPO) material was studied using periodic boundary conditions leading to the finding that at low loadings methanol is not protonated in H-SAPO-34 [95]. Kang et al. confirmed this observation comparing periodic results with an 8T finite cluster approach [96]. In this paper, we report calculated adsorption properties of methanol and ethanol in H-SAPO-34 using large finite clusters and including dispersive interactions.

The theoretically obtained adsorption position of methanol and ethanol is schematically shown in Fig. 2. In correspondence with earlier calculations we also find that methanol exists in its neutral form as a hydrogen-bonded complex. The alcohol is adsorbed end-on bridging across the silicon atom. Three hydrogen bonds are formed: a strong one between the acid proton and the methanol oxygen and two weaker bonds between the methanol hydroxyl proton and a zeolite oxygen. Obtained bond lengths of optimized adsorbed methanol and ethanol are very similar, as can be seen from Fig. 2. We computed corresponding physisorption energies (listed in Table 1). Similar to a previous theoretical study involving the adsorption of methanol in H-ZSM-5, it is seen

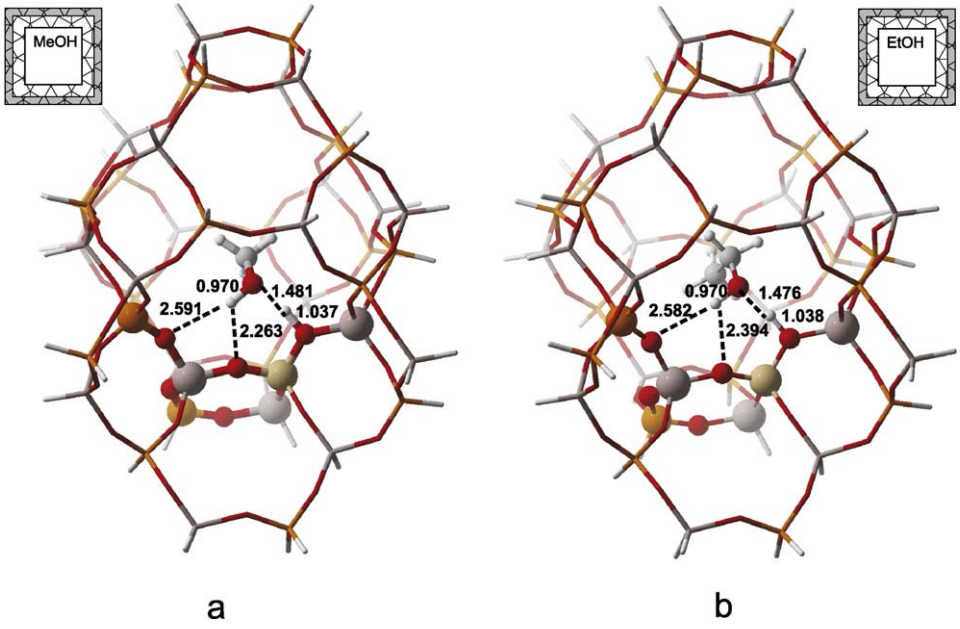

Fig. 2. Representation of physisorbed methanol (a) and ethanol (b) in a SAPO 44T cluster. O–H bond lengths are given in Å.

Table 1
Theoretical physisorption energies ΔE_{phys} of methanol and ethanol in a SAPO 44T cluster, calculated using the ONIOM(B3LYP/dgtzvp:HF/dgtzvp) level of theory within the PHVA scheme. The electronic energies, Zero Point Vibrational Energies (ZPVE) and Van der Waals corrections (vdw) are separately listed. All values in kJ mol^{-1}.

	Electronic energies	ZPVE	vdw	Total
Methanol	−58.94	4.21	−31.14	−85.88
Ethanol	−59.95	3.32	−42.81	−99.44

that the contribution from dispersion interactions is crucial and determines the relative adsorption between both compounds. The difference between the final adsorption energy of methanol and ethanol equals 14 kJ mol^{-1}, the larger alcohol being more strongly adsorbed. This is in agreement with available experimental as well as periodic DFT-D results for adsorption in H-ZSM-5 where the adsorption energies are −115 and −130 kJ mol^{-1} for methanol and ethanol, respectively [97,98]. Overall, the linear increase of adsorption enthalpies with chain length is well-documented for the series of *n*-alkanes [99–107]. The actual increase (generally between 10 and 15 kJ mol^{-1} per added CH_2 group) depends on the zeolite type; the zeolite with the smallest pore diameter shows the largest increase.

3.2. Methanol and ethanol conversion over H-SAPO-34: theoretical and experimental IR spectra

3.2.1. IR spectra of the fresh H-SAPO-34 sample

The experimental DRIFT spectrum of the fresh H-SAPO-34 catalyst in the $\nu(O_zH_z)$ region is reported in Fig. 3(a) (the spectrum in the vibrational range 4000–1000 cm^{-1} is included in Supporting Information). Two peaks can be distinguished at 3615 and at 3593 cm^{-1} and these are usually referred to as the high-frequency (HF) and low-frequency (LF) bands [108]. It has previously been demonstrated that these bands originate from Brønsted acid sites located at different crystallographic positions, and in particular the O(4) and O(2) positions, respectively [108]. This nomenclature (employed in e.g. Refs. [19,109,110]) is clarified for our finite cluster in Fig. 3(b). The chabazite structure consists of double six-ring units linked to give a three-dimensional channel network with eight-ring apertures and the topology of the SAPO material allows for four distinct structural positions of the acid sites. Fig. 3(b) shows that in our calculations for the alcohol adsorption the acid site is

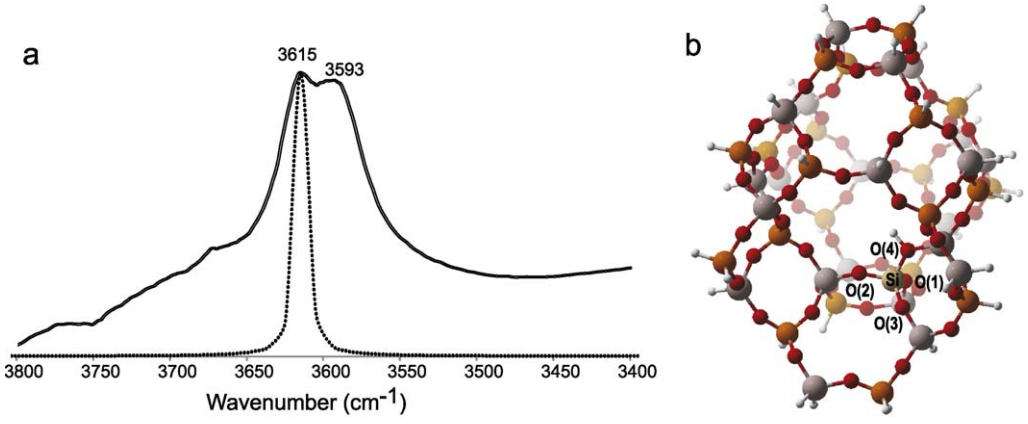

Fig. 3. (a) Experimental DRIFT (solid line) and theoretical (dashed line) spectrum of the fresh H-SAPO-34 sample in the region 3800–3400 cm^{-1}. All theoretical frequencies are scaled with an overall scale factor of 0.9641. (b) Framework H-SAPO-34 44T cluster with indication of the four distinct oxygen sites O(1)–O(4).

Table 2
Calculated harmonic frequencies of the empty H-SAPO-34 44T cluster and of the cluster loaded with a physisorbed methanol or ethanol. Values in cm^{-1}.

	ν (CH)	δ (CH)	δ (CH_3)	ν (OH)	ν (O_zH_z)	δ_i (O_zH_z)	δ_o (O_zH_z)
H-SAPO-34					3615	1084	374
Methanol							
Gas phase	2888–3006	1441–1452	1423	3678			
In sapo	2928–3041	1439–1456	1414	3579	2332	1449	1070
Ethanol							
Gas phase	2877–3001	1394–1469	1353	3674			
In sapo	2921–3016	1441–1465	1369	3594	2306	1453	990

located at the O(4) position which belongs to one 4T and two 8T rings. The calculated frequency value of the O_zH_z stretching vibration of the acid proton with the framework oxygen in an empty framework was fitted towards the experimentally obtained HF peak at 3615 cm^{-1} resulting in a scaling factor of 0.9641 which is used throughout the manuscript. Our results are in line with data reported by Martins et al., indicating peak maxima at 3631, 3617 and 3600 cm^{-1}[110,111]. In addition to the HF and LF band, the third band (3617 cm^{-1}) was attributed – combining FTIR and ^{29}Si MAS NMR data – to strong acidic protons present either at the borders of silica patches/islands or inside aluminosilicate domains. Although present in the applied experimental sample (see Section 2.2) modeling of such acid sites is outside the scope of the present paper; in the present cluster calculations we mainly focus on the local environment (steric limitations of the pore topology) around one isolated Si site. Finally, we note that the spectrum of the fresh sample will be used as background for all other experimental DRIFT spectra.

3.2.2. Adsorption of methanol and ethanol

We calculated IR spectra of adsorbed methanol and ethanol in a SAPO cluster (Fig. 2). An overview of all important modes is given in Table 2, together with the characteristic frequencies of the empty SAPO cluster and those of methanol and ethanol in the gas phase. The most notable difference upon adsorption of the alcohols and the fresh H-SAPO-34 sample is observed for the O–H stretching modes. The ν (O_zH_z) corresponding to the framework Brønsted acid site is redshifted to low frequencies, giving rise to highly resolved peaks at 2332 (methanol) and 2306 (ethanol) cm^{-1}, whereas the nearly free ν (OH) of the alcohols is observed at 3579 (methanol) and 3594 (ethanol) cm^{-1}. Compared to the gas phase O–H frequency the original frequency at 3678 and 3674 cm^{-1} is redshifted with approximately 100 and 80 cm^{-1} for methanol and ethanol, respectively, due to the hydrogen-bonding with oxygen frameworks. The in- (δ_i) and out- (δ_o) of-plane bending of the acid proton also changes substantially; the frequencies are blue-shifted to 1449–1453 and 1070–990 cm^{-1}. The δ_i (O_zH_z) values now fall in the C–H bending region. The observations are quite similar for both alcohols. The bending modes of the hydrocarbon chains (δ (CH) and δ (CH_3)) remain almost unaltered upon physisorption of the alcohols and the C–H stretchings shift minorly to higher frequencies. The identification of the separate modes is often ambiguous due to coupling between nearby-lying modes. In Section 3.3 we will discuss a theoretical procedure to separate the various contributions.

The theoretical observations are now linked with experimental data. Fig. 4 displays the spectra recorded after 5 and 10 s (representing the initial adsorption stage of the alcohol) in the high-frequency vibrational range 4000–2200 cm^{-1} since the most striking features are observed in the O–H stretching region. In Fig. 4 the calculated peaks are also indicated. A broad band is growing starting from 3500 cm^{-1}, with maxima at 3495 (methanol) and 3505 (ethanol) cm^{-1}. This absorption at about 3500 cm^{-1} is due to the nearly free ν (OH) mode of methanol. Theoretically this mode is located at 3579 (methanol) and 3594 (ethanol) cm^{-1}, in fairly good agreement with experiment. The progressive appearance of a broad absorption in the range 3500–3050 cm^{-1} range can also originate from H-bonded reactants with P–OH, Al–OH and Si–OH species which are not modeled in the theoretical simulations [36,112]. Similarly, several signals observed around 3800 cm^{-1} also indicate the presence of Al–OH bonds [113]. In the region 2500–2000 cm^{-1} broad peaks are observed which are growing with increasing doses of alcohol. These bands relate to the vibration of the acid proton, which was also theoretically shown to be present in this region (peaks at 2332 and 2306 cm^{-1} for methanol and ethanol, respectively, see Fig. 4). It is also seen that the in situ experimental spectra in this region are severely influenced by additional framework vibrations. These framework vibrations are not expected based on the theoretical data, although application of the PHVA–MBH analysis scheme (see Section 3.3.3) will rationalize that even the skeleton vibrations are susceptible upon adsorption of guest molecules. The experimental C–H stretching vibrations originating from CH_2 and CH_3 groups are at similar positions for both alcohols and clearly visible at 2980, 2927 and 2870 cm^{-1} for methanol and 2976, 2932 and 2880 cm^{-1} in case of ethanol [114]. The calculated peak positions are slightly too much blue-shifted compared with experiment. The experimental spectra of Fig. 4 are in correlation with previously reported transmission FTIR spectra recorded by Bordiga et al. who analyzed in detail the adsorption of increasing dosages of methanol on both H-SSZ-13 and H-SAPO-34 (at 300 K) and who reported the continuous growth of the ABC triad [36]. It is noteworthy to men-

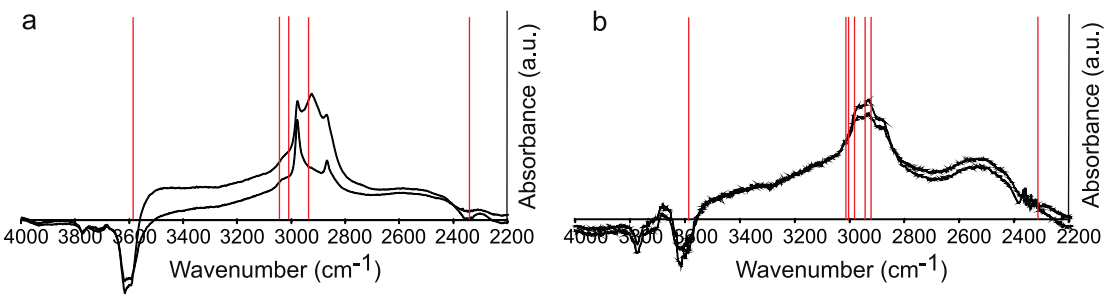

Fig. 4. Experimental DRIFT spectra (in black) and calculated peak positions (in red) for methanol (a) and ethanol (b) adsorption in H-SAPO-34. The experimental spectra are taken after 5 and 10 s. (For interpretation of the references to color in this figure legend, the reader is referred to the web version of the article.)

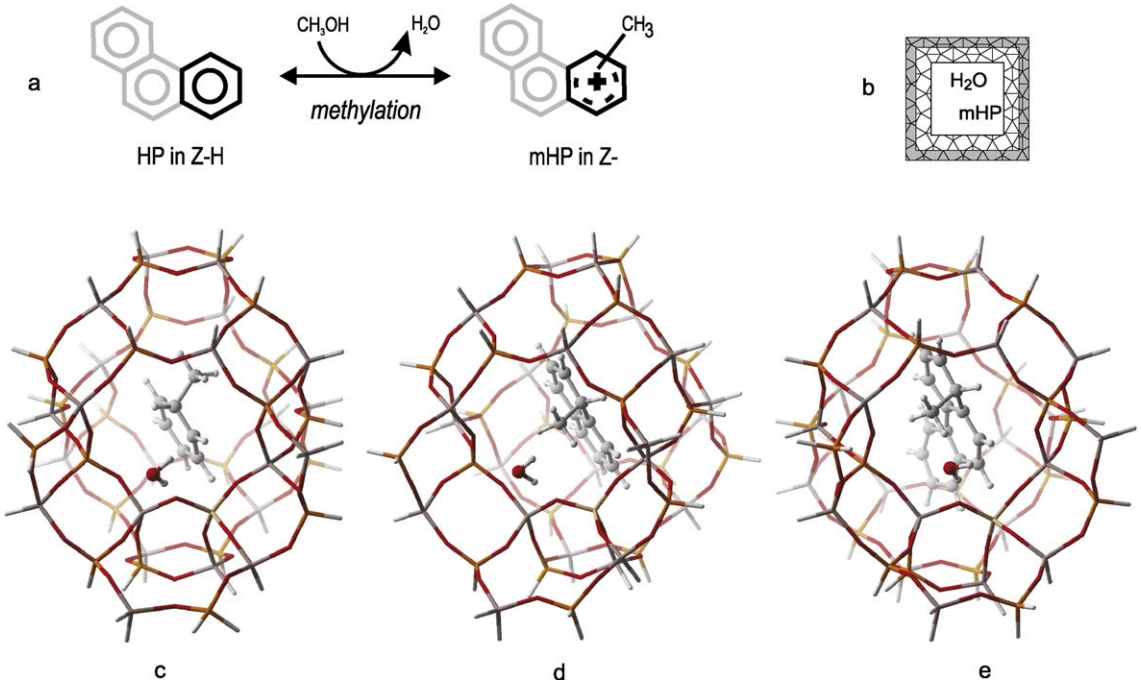

Fig. 5. Schematic representation of methylation reactions of an HP species (a), applied scheme for the geometry optimization and NMA (b), optimized structures at the ONIOM(B3LYP/dgtzvp:MNDO) level of theory of **mB** (c), **mN** (d) and **mPH** (e) in a SAPO cluster. The water molecule formed during the methylation reaction is also shown.

tion that improvement of the theoretical values can be obtained by explicitly taking into account anharmonicities, as shown by Mihaleva et al. for the adsorption of water in CHA [115].

3.2.3. *Formation of hydrocarbon pool species*

In addition to the adsorbed C_1 and C_2 alcohols, (poly)aromatic carbonaceous compounds entrapped within the zeolitic pore are also investigated. For sake of clarity, we restrict the discussion to singly methylated aromatic cations; these species represent carbonaceous compounds which can be further methylated to active HP species and further degrade to coke-like molecules. The thermodynamics and kinetics of methylation reactions of naphthalene and its derivatives were previously studied from a theoretical viewpoint [19], however the corresponding IR spectra of these species are investigated here for the first time. Simulations are performed on a SAPO 44T cluster loaded with a methylated benzenium (**mB**), naphthalenium (**mN**) and phenanthrenium (**mPH**) ion, respectively. These structures are assumed to be actual reaction products resulting from methylation via methanol (Fig. 5(a)) including the formed water molecule. The optimized geometries (at the ONIOM(B3LYP/dgtzvp:MNDO) level of theory) of the methylated aromatic cations are also included in Fig. 5(c)–(e). It is interesting to see that in the case of **mB** the molecule has been submitted to a rotation during the geometry optimization indicating that this small molecule encounters little steric hindrance within the pore. For the cases involving two or three aromatic rings, the bulkier structure is more confined and rotation is hence severely hampered [116].

Corresponding calculated IR spectra are depicted in Fig. 6. The spectra are reported in the interesting vibrational ranges between 1700 and 1300 (ν (C=C) and δ (CH)) and 3300–2800 cm^{-1} (ν (CH)). Calculated harmonic frequencies are also tabulated in Table 3. Focussing on the ν (CH) modes, we differentiate between the aromatic and aliphatic hydrogen atoms. The IR intensity of the first group is much higher (Fig. 6(a)) compared to the second one since the computed species are only singly methylated compounds. The computed frequencies are overall found to be higher for the species in the zeolitic environment and increase with the size of the aro-

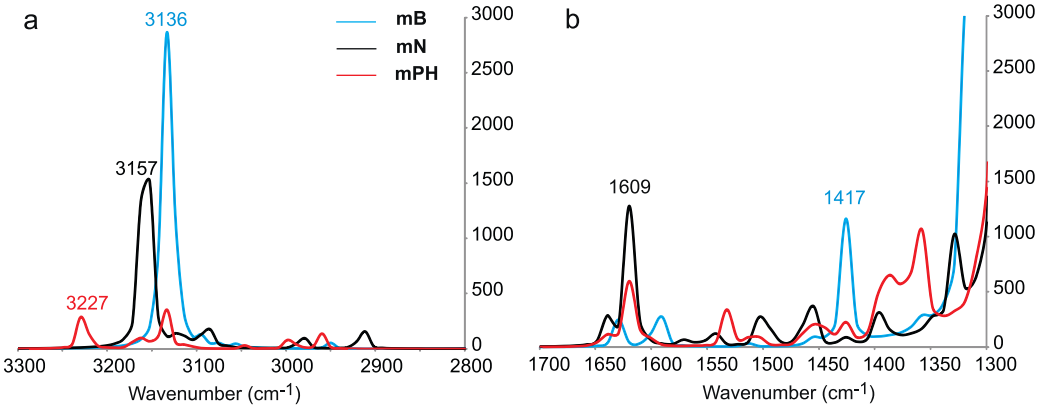

Fig. 6. Calculated IR spectra of **mB**, **mN** and **mPH** enclosed in an SAPO 44T cluster in the ν (CH) vibrational range 3300–2800 cm^{-1} (a) and ν (C=C) vibrational range 1700–1300 cm^{-1} (b). Peak maxima are indicated.

Table 3
Calculated harmonic frequencies for the singly methylated aromatic cations in gas phase and loaded in the SAPO 44T cluster. Values in cm^{-1}.

	$\nu_{aromatic}$ (CH)	ν_{methyl} (CH)	ν_{proton} (CH)	ν (C=C)
mB				
Gas phase	3070–3098	2952–3039	2796	1430–1576
In sapo	3057–3136	2952–3044	2788	1417–1584
mN				
Gas phase	3062–3099	2949–3038	2857	1338–1593
In sapo	3082–3157	2982–3091	2915	1449–1609
mPH				
Gas phase	3067–3100	2947–3035	2873	1323–1587
In sapo	3126–3227	2960–3110	2995	1453–1636

matic. An analogous behavior is found for the frequencies of the additional methyl group (ν_{methyl} (CH)). Both regions are clearly separated from each other. In addition, the C–H stretching of the extra proton (ν_{proton} (CH)) can also clearly be observed since it lies at lower frequency values; except for the **mPH** compound in SAPO where this mode is located in between the ν_{methyl} (CH) stretches. The ν (C=C) band consists of various peaks, the values of the gas phase cations are also lower compared to those in the SAPO 44T cluster. It is seen that in the case of **mB** a peak maximum is identified at 1417 cm^{-1}, whereas in the case of **mN** and **mPH** the maximum is observed at 1610 cm^{-1}.

The alcohol to hydrocarbon conversion is now further experimentally explored using DRIFT spectroscopy. The spectra of adsorbed and retained materials are recorded as a function of time and the results are given in Fig. 7 for similar regions as the theoretical spectra in Fig. 6. After reaction, darkening of the samples is observed, in particular a yellowish and greyish coloration in the case of methanol and ethanol, respectively. Whereas the comparison between methanol and ethanol is made for some selected zeolites (in particular H-Y, H-ZSM-5 and H-mordenite) [112], this is the first study to compare IR spectra of both alcohols over H-SAPO-34.

Fig. 7 shows that the addition of methanol and ethanol to SAPO-34 provides overall similar vibrational spectra. Nevertheless, shifts in peak positions and clear variations in relative intensities are observed when the C_1 and C_2 alcohol conversions are carefully compared. Our experimental results agree with previous detailed studies [37,38] as well as with the simulated spectra. With increasing alcohol coverage, the acid sites at 3615 and 3620 cm^{-1} for methanol and ethanol, respectively progressively erode (see Fig. 4 and the full DRIFT spectra in Supporting Information) [36,112,117]. In Fig. 7(a) and (c) the progressive growth and overall broadening of the C–H region is indicative for the formation of alkylated aromatics with increasing substitution. The formation of bands at 3025 and 3060 cm^{-1} for methanol and ethanol respectively, advocates the formation of aromatic C–H vibrations. Especially in the case of ethanol, bands arise at higher frequencies and the theoretical values listed in Table 3 suggest that these might also originate from larger aromatic compounds. This is accompanied by growth of the C= C band at 1607 cm^{-1} with shoulder at 1640 cm^{-1} for methanol and 1600 cm^{-1} with shoulder at 1660 cm^{-1} for ethanol (see Fig. 7(b) and (d)) which also demonstrate the formation of aromatic carbenium ions as suggested in literature earlier [38,37,118–120] and is in line with the calculated IR spectra of Fig. 6(b). Once formed,

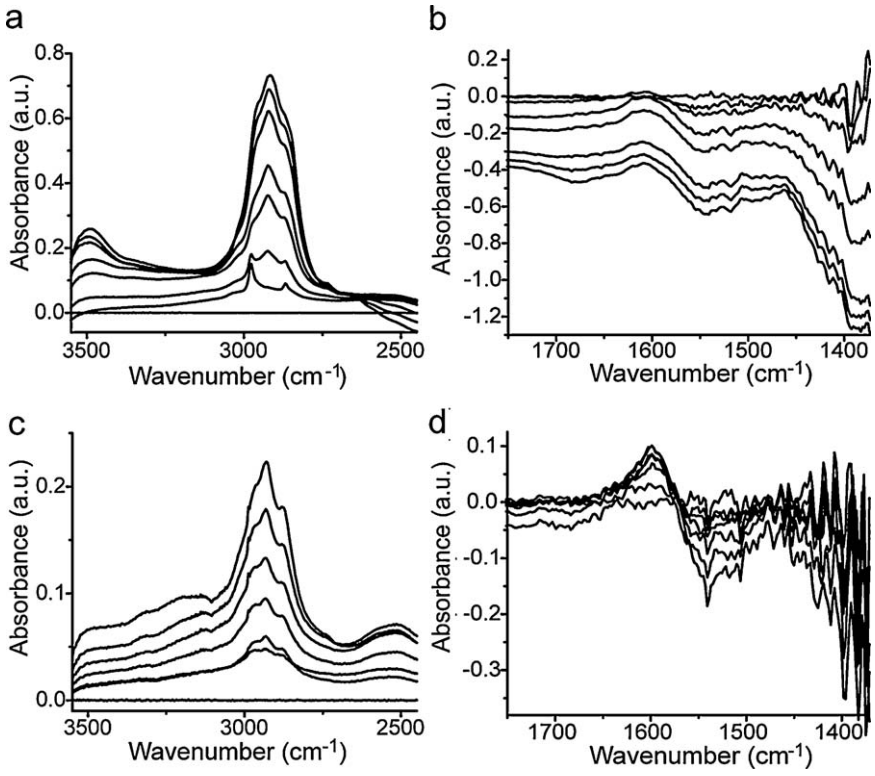

Fig. 7. Selection of the time-resolved DRIFT spectra recorded during the methanol (a and b) and ethanol (c and d) conversion over H-SAPO-34 at 300 °C. The illustrated spectra are background-subtracted.

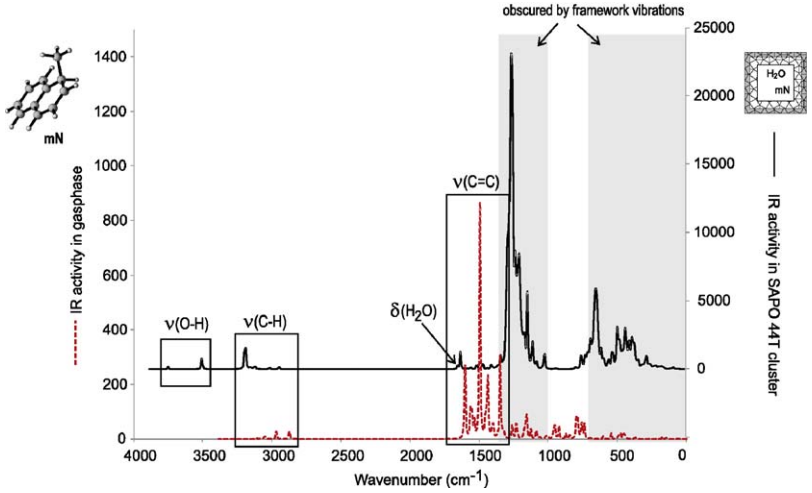

Fig. 8. Calculated IR spectra (scaled with 0.9641) of **mN** in gasphase (red dashed line) compared with in a SAPO 44T cluster (black solid line). In some frequency regions (grey shaded) the **mN** spectrum is mixed up with framework vibrations. (For interpretation of the references to color in this figure legend, the reader is referred to the web version of the article.)

these bands remain rather stable throughout the entire period of reaction though the relative stronger intensity in the case of ethanol is evident.

3.3. Advanced normal mode analysis to explore vibrational spectra

Particular regions of the vibrational range of the full framework–guest spectrum are obscured by the skeletal modes of the zeolite, as is illustrated for **mN** in Fig. 8. The calculated IR spectrum of a gasphase species is compared with that of the same species entrapped in the SAPO cluster. The vibrational modes of the extra water molecule in the cluster are of course absent for the gasphase molecule. In order to overcome this shortcoming, we present a new theoretical procedure which will enable to unravel the vibrational spectra and which can for example filter out the zeolitic framework vibrations.

3.3.1. NMA of adsorbed methanol

We analyze in detail the computed vibrational spectrum of methanol adsorbed in the SAPO 44T cluster (see Fig. 2), which was already discussed in Section 3.1. An overview of the results is given in Fig. 9. Panel (a) depicts the computed d.o.s. spectrum for the full system, i.e. the SAPO framework with adsorbed methanol, using the $PHVA_H$ scheme (minimal fixed region). When computing the cumulative overlap between the modes with model $PHVA_H$ versus model $PHVA_H$–MBH_{MeOH} (where the internal modes of methanol are kept fixed), the framework modes remain well reproduced by the second model leading to high cumulative overlaps, while the methanol modes are absent leading to low cumulative overlaps. In practice it is more instructive to consider the complementary cumulative overlap, i.e. $1 - O_i$ (see Eq. (1)) expressed in percentages. To illustrate: the internal vibrations of methanol are absent in the $PHVA_H$–MBH_{MeOH} spectrum. The peaks around 3000 and 3700 cm^{-1} in Fig. 9(a) and (c) represent the C–H and O–H stretches of methanol, respectively. They have no cumulative overlap with modes of the $PHVA_H$–MBH_{MeOH} scheme and hence are displayed as 100% lines in the complementary cumulative overlap plot depicted in Fig. 9(b). The vertical lines are positioned at the vibrations according to the $PHVA_H$ model. This plot can be superimposed on the original $PHVA_H$ spectrum in order to locate the methanol frequencies (resulting in panel (d)). Hence the cumulative overlap can serve as a technique to identify the character of the modes by comparing different PHVA and PHVA–MBH schemes. Similarly, when the plot in Fig. 9(b) is superimposed on the gas phase spectrum of methanol (c), the shifts of the internal methanol frequencies induced by the SAPO framework become visible (see Fig. 9(e)). Using the PHVA–MBH technique it is easy to see that the positions of particular peaks have changed substantially upon adsorption. The ν (OH) stretch exhibits a redshift of 100 cm^{-1}, whereas the ν (CH) modes shift to higher frequencies with an average value of 46 cm^{-1} (see also Table 2).

3.3.2. NMA of adsorbed naphthalene

A similar analysis has been performed for the adsorption of pure naphthalene (**N**). By means of the cumulative overlap, the influence of the adsorption is visualized in Fig. 10. Characteristic frequency ranges are given (similar to those examined for the singly methylated aromatic cations in Fig. 6): 1700–1300 cm^{-1} and 3300–2800 cm^{-1}. The cumulative overlap considered here involves the $PHVA_H$ and $PHVA_H$–MBH_N scheme. In the latter scheme, the internal vibrations of naphthalene are missing, such that modes mainly consisting of naphthalene vibrations have a low value of the cumulative overlap, which translates into a high value of the complementary cumulative overlap. In Fig. 10 the vertical lines corresponding to the complementary cumulative overlap all have very high values (between 98 and 100%) in the selected frequency ranges, indicative of their pure naphthalenic character. The complementary cumulative overlap is superimposed onto the gas phase spectrum. This clearly shows a consistent non-negligible shift of the gas phase naphthalene frequencies to higher values upon adsorption. The average shift is higher in the high frequency spectrum: in the ν (C=C) an average frequency shift of 12 cm^{-1} is obtained (Fig. 10(a)), whereas this increases to 44 cm^{-1} for the ν (CH) region (Fig. 10(b)). The overall qualitative picture is in accordance with the results in Section 3.2.3 where for the singly methylated aromatic cations the comparison was made between frequencies of gas phase compounds versus those upon adsorption in the SAPO cluster (see in particular Table 3), however application of the PHVA–MBH method enables an easier and more transparent approach.

3.3.3. NMA of the SAPO 44T model cluster

The PHVA–MBH method is applied to investigate the influence of guest molecules on the vibrations of the zeolitic framework. We therefore traced the SAPO frequencies for a series of adsorbed guests. In Fig. 11 the reference is the spectrum of the empty SAPO structure (a), calculated with the minimal fixed atom region

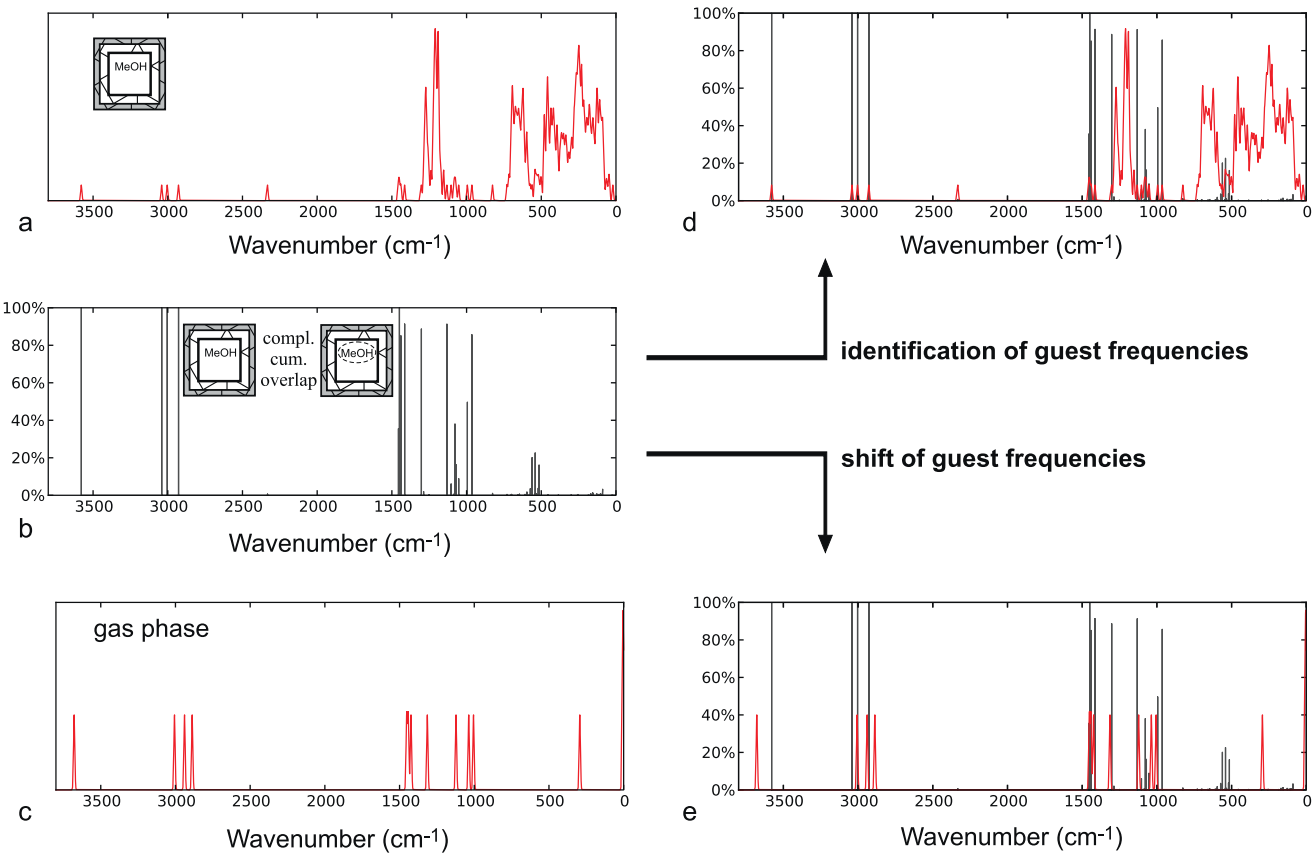

Fig. 9. Methodology to unravel calculated spectra with NMA for the case of methanol adsorbed in a SAPO 44T cluster. (a) The overall d.o.s. spectrum calculated with the minimal fixed region, $PHVA_H$. (b) Complementary cumulative overlap (compl. cum. overlap in %) of the $PHVA_H$ and $PHVA_H$–MBH_{MeOH} models indicate the location of the methanol frequencies. The vertical lines are positioned at the vibrations according to the $PHVA_H$ model. (c) The d.o.s. spectrum of methanol in the gas phase calculated with the standard full NMA. (d) Superposition of plots (a + b) allows identification of the methanol frequencies. (e) Superposition of plots (b + c) visualizes the frequency shifts between methanol in the gas phase and methanol adsorbed in H-SAPO-34.

($PHVA_H$). The skeleton vibrations are located in the intervals 750–0 and 1300–1020 cm^{-1}; both regions are well-separated by a clear gap (see also Fig. 8). In the remaining plots of Fig. 11, the following species are adsorbed: (b) methanol, (c) naphthalene, (d and e) both naphthalene and methanol in the reactant and transition state of an actual methylation reaction (see Fig. 5(a)) and (f) methylated naphthalene and formed water, i.e. the product state of the methylation step. The cumulative overlap between the $PHVA_H$ and $PHVA_{sapo}$ models is considered here. The latter NMA scheme leads to the calculation of only the guest frequencies since all zeolite atoms are constrained. In Fig. 11 the complementary cumulative overlap is plotted, and hence the positions with a high value (represented by a large vertical line) are those with a high framework character. Panels (b–f) indicate that the SAPO frequencies shift little such that a decoupling of the framework modes on one hand and the modes of the guest molecules on the other is a fair first approximation. However, for the actual reaction intermediates (b–d) it is seen that framework modes are observed in the region 1020–750 due to the strong coupling with the guest molecules. For the reactant state (Fig. 11(d)) a peak around 800 cm^{-1} is found and for the transition (Fig. 11(e)) and product (Fig. 11(f)) state a few SAPO frequencies are located at values around 1000 cm^{-1}. Visualization of these vibrational modes revealed that they correspond to the asymmetric Al–O–Si stretch of the structural acid site which couples strongly with the out-of-plane C–H modes of the aromatic HP compound. When investigating the frequency range

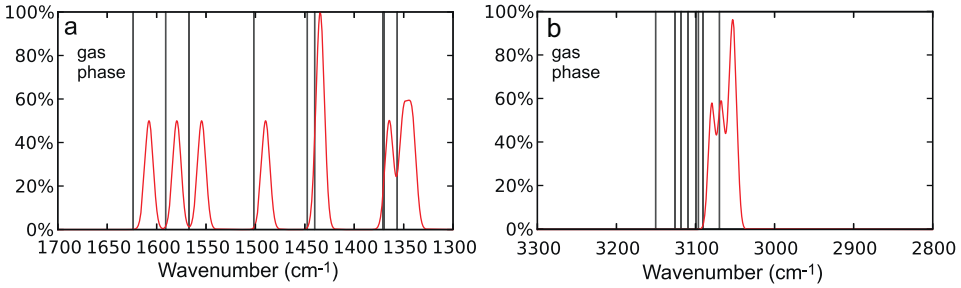

Fig. 10. Influence of adsorption in SAPO on the calculated naphthalene spectrum for the ν(C=C) range between 1700 and 1300 cm^{-1} (a) and the ν(CH) range between 3300 and 2800 cm^{-1} (b). The d.o.s. of a gas phase naphthalene molecule is given in red. The vertical lines correspond with the complementary cumulative overlap of the $PHVA_H$ and $PHVA_H$–MBH_N models, indicating the vibrations of the naphthalene compound. Adsorption induced shift of the frequencies with respect to the gas phase spectrum are observed. (For interpretation of the references to color in this figure legend, the reader is referred to the web version of the article.)

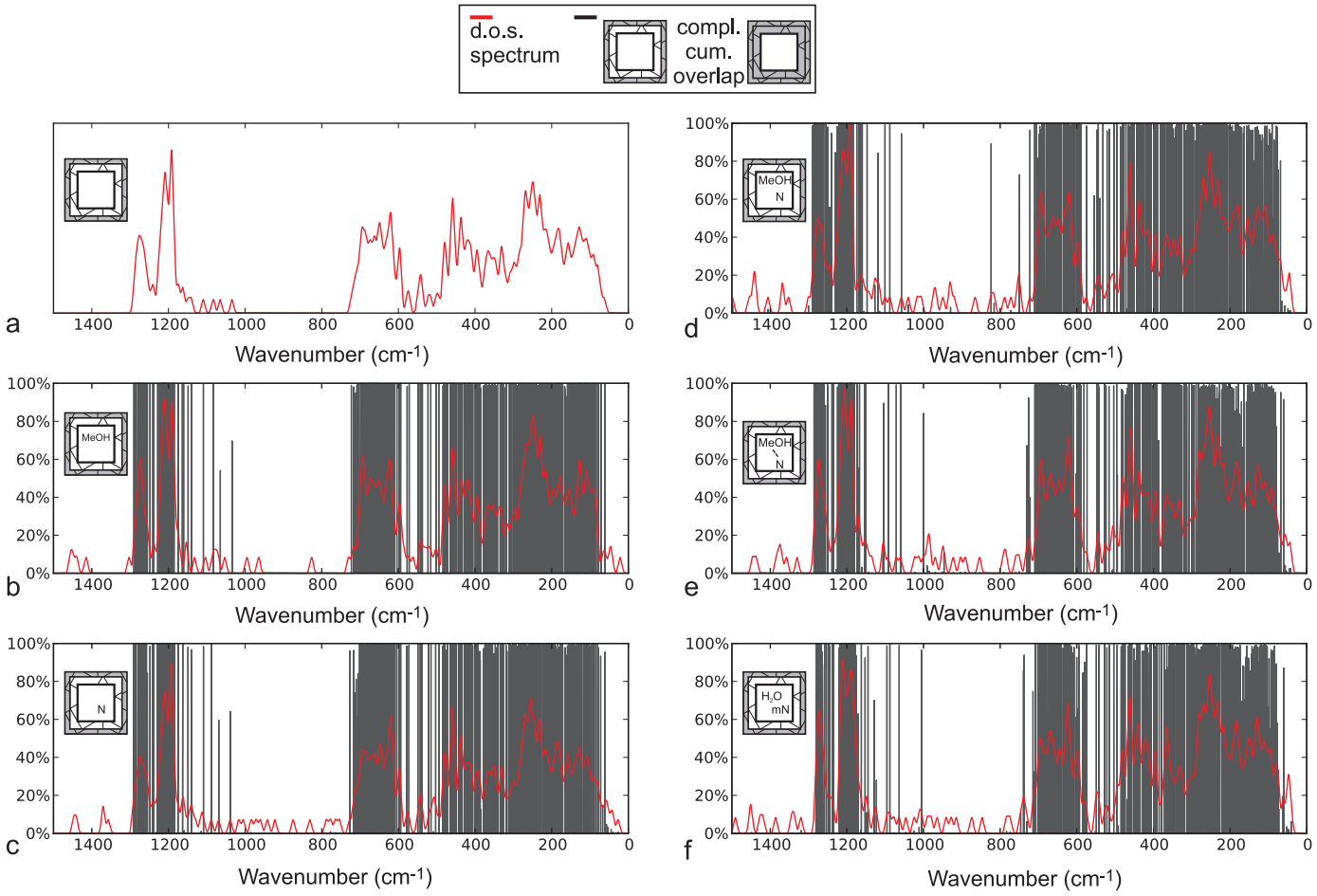

Fig. 11. Influence of adsorption on the calculated SAPO spectrum is investigated with NMA and the cumulative overlap in the lower part of the spectrum (1500–0 cm^{-1}). The d.o.s. are plotted in red. (a) The spectrum of empty SAPO calculated with the minimal fixed atom region, $PHVA_H$. Identification of SAPO frequencies in (b) sapo plus methanol, (c) sapo plus naphthalene, (d and e) sapo plus naphthalene and methanol in the reactant and transition state and (f) sapo plus methylated naphthalene and water. (For interpretation of the references to color in this figure legend, the reader is referred to the web version of the article.)

around 800 and 1000 cm^{-1}, one should be aware of the fact that some modes are no pure guest vibrations but also include some SAPO vibrations. We note that for the cases investigated here, the overlap between the framework and guest modes is still minimal. The PHVA–MBH method can provide more detailed information in these cases where the characteristic frequencies of the guest molecules lie exactly within the range of the skeleton vibrations, which is for instance the case for amines (characteristic C–N stretch lies between 1360 and 1080 cm^{-1}).

4. Conclusions

The conversion of methanol and ethanol over H-SAPO-34 is a very complex mechanism for which theoretical spectroscopic data can aid the interpretation of the experiments. In this paper, theoretical and experimental IR results have been discussed. For the theoretical simulations a large finite cluster was applied to mimic the zeolitic pore and parts of the environment. The initial physisorption of the alcohols in the SAPO material was modeled and calculated adsorption energies indicate that ethanol is adsorbed more strongly compared to methanol by almost 14 kJ mol^{-1}. Corresponding calculated IR spectra indicate that both alcohols behave in a similar way, which is in agreement with the experimental in situ DFRIFT measurements. Framework–guest interactions, mainly due to hydrogen bonding, result in a clear redshift of the OH stretching vibration of the Brønsted acid site. The alcohol conversion over H-SAPO-34 results in the formation of carbonaceous compounds in the zeolitic pore and singly methylated aromatic cations are taken as representatives. Computed IR spectra of these species adsorbed on H-SAPO-34 point out that the characteristic C= C vibrations of the larger aromatic HP compounds exhibit a peak with maximal IR intensity at 1610 cm^{-1}, which is in agreement with experimentally observed bands at 1607 and 1600 cm^{-1} for methanol and ethanol, respectively.

Particular frequency regions are obscured due to the overlap of guest and framework vibrations. In order to overcome this deficiency, an advanced normal mode analysis, based on the PHVA and PHVA–MBH schemes, has been presented to analyze the computed vibrational spectra. The use of a particular block filters out the internal modes of this block. A cumulative overlap function comparing different NMA models has been defined. It can be used to identify the character of individual modes as well as visualize frequency shifts when comparing spectra of compounds in the gas phase versus entrapped in a zeolitic environment. It is found that the SAPO skeleton vibrations are relatively unaffected upon adsorption, although exceptions are reported originating from the strong coupling between the asymmetric Al–O–Si stretch and the C–H out-of-plane bending of entrapped hydrocarbons. Moreover, loading of a SAPO framework with methanol and naphthalene result in non-negligible peak shifts due to the framework–guest interactions. In the case of the aromatic hydrocarbon, an average peak shift of 12 and 44 cm^{-1} is reported for the ν (C=C) and ν (CH), respectively.

One should hence be careful to assign experimental peaks based on simulated gas phase data.

In general, the combined PHVA–MBH analysis procedure has the potential to become a valuable tool to explore computed vibrational spectra and the obtained information can in turn serve as a reference to assign peaks of complex experimental spectra. The advanced normal mode analysis enables a systematic separation of the framework–guest vibrational modes and it can describe induced peak shifts upon adsorption in a nanoporous environment.

Acknowledgments

We wish to acknowledge the Fund for Scientific Research – Flanders (FWO), the Research Board of Ghent University, and BELSPO in the frame of IAP/6/27. Funding was also received from the European Research Council under the European Community's Seventh Framework Programme [FP7(2007–2013) ERC grant agreement number 240483]. Computational resources and services used in this work were provided by Ghent University. This work was also supported by the Dutch National Science Foundation (NWO-CW VICI and TOP subsidies to B.M.W) and the National Research School Combination Catalysis (NRSC-C).

Appendix A. Supplementary data

Supplementary data associated with this article can be found, in the online version, at doi:10.1016/j.cattod.2011.05.040.

References

[1] M. Stocker, Micropor. Mesopor. Mater. 29 (1999) 3.
[2] J.F. Haw, W.G. Song, D.M. Marcus, J.B. Nicholas, Acc. Chem. Res. 36 (2003) 317.
[3] I.M. Dahl, S. Kolboe, Catal. Lett. 20 (1993) 329.
[4] I.M. Dahl, S. Kolboe, J. Catal. 149 (1994) 458.
[5] I.M. Dahl, S. Kolboe, J. Catal. 161 (1996) 304.
[6] W.G. Song, D.M. Marcus, H. Fu, J.O. Ehresmann, J.F. Haw, J. Am. Chem. Soc. 124 (2002) 3844.
[7] R.M. Dessau, J. Catal. 99 (1986) 111.
[8] S. Svelle, F. Joensen, J. Nerlov, U. Olsbye, K.P. Lillerud, S. Kolboe, M. Bjorgen, J. Am. Chem. Soc. 128 (2006) 14770.
[9] M. Bjorgen, F. Joensen, K.P. Lillerud, U. Olsbye, S. Svelle, Catal. Today 142 (2009) 90.
[10] D.M. McCann, D. Lesthaeghe, P.W. Kletnieks, D.R. Guenther, M.J. Hayman, V. Van Speybroeck, M. Waroquier, J.F. Haw, Angew. Chem. Int. Ed. 47 (2008) 5179.
[11] D. Lesthaeghe, A. Horre, M. Waroquier, G.B. Marin, V. Van Speybroeck, Chem. Eur. J. 15 (2009) 10803.
[12] D. Lesthaeghe, J. Van der Mynsbrugge, M. Vandichel, M. Waroquier, V. Van, Speybroeck, ChemCatChem 3 (2011) 208.
[13] M. Bjorgen, F. Bonino, S. Kolbie, K.P. Lillerud, A. Zecchina, S. Bordiga, J. Am. Chem. Soc. 125 (2003) 15863.
[14] W.G. Song, J.F. Haw, J.B. Nicholas, C.S. Heneghan, J. Am. Chem. Soc. 122 (2000) 10726.
[15] J.F. Haw, D.M. Marcus, Top. Catal. 34 (2005) 41.
[16] C.M. Wang, Y.D. Wang, Z.K. Xie, Z.P. Liu, J. Phys. Chem. C 113 (2009) 4584.
[17] C.M. Wang, Y.D. Wang, H.X. Lie, Z.K. Xie, Z.P. Liu, J. Catal. 271 (2010) 386.
[18] W.G. Song, H. Fu, J.F. Haw, J. Phys. Chem. B 105 (2001) 12839.
[19] K. Hemelsoet, A. Nollet, V. Van Speybroeck, M. Waroquier, Chem. Eur. J. (2011), doi:10.1002/chem.201100920.
[20] S. Teketel, U. Olsbye, K.P. Lillerud, P. Beato, S. Svelle, Micropor. Mesopor. Mater. 136 (2010) 33.
[21] Y. Kumita, J. Gascon, E. Stavitski, J.A. Moulijn, F. Kapteijn, Appl. Catal. A 391 (2011) 234.
[22] F.F. Madeira, N.S. Gnep, P. Magnoux, S. Maury, N. Cadran, Appl. Catal. A 367 (2009) 39.
[23] F.F. Madeira, N.S. Gnep, P. Magnoux, H. Vezin, S. Maury, N. Cadran, Chem. Eng. J. 161 (2010) 403.
[24] I.M. Dahl, R. Wendelbo, A. Andersen, D. Akporiaye, H. Mostad, T. Fuglerud, Micropor. Mesopor. Mater. 29 (1999) 159.
[25] H. Fu, W.G. Song, J.F. Haw, Catal. Lett. 76 (2001) 89.
[26] B.P.C. Hereijgers, F. Bleken, M.H. Nilsen, S. Svelle, K.P. Lillerud, M. Bjorgen, B.M. Weckhuysen, U. Olsbye, J. Catal. 264 (2009) 77.
[27] D. Mores, E. Stavitski, M.H.F. Kox, J. Kornatowski, U. Olsbye, B.M. Weckhuysen, Chem. Eur. J. 14 (2008) 11320.
[28] D. Mores, J. Kornatowski, U. Olsbye, B.M. Weckhuysen, Chem. Eur. J. 17 (2011) 2874.
[29] D.S. Wragg, R.E. Johnsen, M. Balasundaram, P. Norby, H. Fjellvag, A. Gronvold, T. Fuglerud, J. Hafizovic, O.B. Vistad, D. Akporiaye, J. Catal. 268 (2009) 290.
[30] A. Corma, Chem. Rev. 95 (1995) 559.
[31] A. Zecchina, C. Lamberti, S. Bordiga, Catal. Today 41 (1998) 169.
[32] S. Coluccia, L. Marchese, G. Martra, Micropor. Mesopor. Mater. 30 (1999) 43.
[33] C. Lamberti, A. Zecchina, E. Groppo, S. Bordiga, Chem. Soc. Rev. 39 (2010) 4951.
[34] L. Marchese, A. Frache, E. Gianotti, G. Martra, M. Causa, S. Coluccia, Micropor. Mesopor. Mater. 30 (1999) 145.
[35] A. Martucci, A. Alberti, G. Cruciani, A. Frache, S. Coluccia, L. Marchese, J. Phys. Chem. B 107 (2003) 9655.
[36] S. Bordiga, L. Regli, C. Lamberti, A. Zecchina, M. Bjorgen, K.P. Lillerud, J. Phys. Chem. B 109 (2005) 7724.
[37] L. Palumbo, F. Bonino, P. Beato, M. Bjorgen, A. Zecchina, S. Bordiga, J. Phys. Chem. C 112 (2008) 9710.
[38] J.W. Park, G. Seo, Appl. Catal. A 356 (2009) 180.
[39] H.O. Pastore, S. Coluccia, L. Marchese, Annu. Rev. Mater. Res. 35 (2005) 351.
[40] E.M. Flanigen, R.L. Patton, S.T. Wilson, Innovation in Zeolite Science, in: P.J. Grobet et al. (Eds.), Stud. Surf. Sci. Catal. 37 (1988) 13.
[41] S.L. Suib, A.M. Winiecki, A. Kostapapas, Langmuir 3 (1987) 483.
[42] C.S. Blackwell, R.L. Patton, J. Phys. Chem. 92 (1988) 3965.
[43] G. Sastre, D.W. Lewis, C.R.A. Catlow, J. Phys. Chem. 100 (1996) 6722.
[44] C. Morterra, G. Magnacca, Catal. Today 27 (1996) 497.
[45] G. Sastre, D.W. Lewis, R.A. Catlow, J. Phys. Chem. B 101 (1997) 5249.
[46] R. Vomscheid, M. Briend, M.J. Peltre, P.P. Man, D. Barthomeuf, J. Phys. Chem. 98 (1994) 9614.
[47] D. Barthomeuf, J. Phys. Chem. 97 (1993) 10092.
[48] A. Buchholtz, W. Wang, M. Xu, A. Arnold, M. Hunger, Micropor. Mesopor. Mater. 56 (2002) 267.
[49] G. Sastre, D.W. Lewis, C.R.A. Catlow, J. Mol. Catal. A 119 (1997) 349.
[50] S. Svelle, C. Tuma, X. Rozanska, T. Kerber, J. Sauer, J. Am. Chem. Soc. 131 (2009) 816.
[51] V. Van Speybroeck, J. Van der Mynsbrugge, M. Vandichel, K. Hemelsoet, D. Lesthaeghe, A. Ghysels, G.B. Marin, M. Waroquier, J. Am. Chem. Soc. 133 (2011) 888.
[52] S.Q. Jin, J.D. Head, Surf. Sci. 318 (1994) 204.
[53] M.D. Calvin, J.D. Head, S.Q. Jin, Surf. Sci. 345 (1996) 161.
[54] J.D. Head, Int. J. Quantum Chem. 65 (1997) 827.
[55] H. Li, J.H. Jensen, Theor. Chem. Acc. 107 (2002) 211.
[56] A. Ghysels, D. Van Neck, M. Waroquier, J. Chem. Phys. 127 (2007) 164108.
[57] A. Ghysels, D. Van Neck, V. Van Speybroeck, T. Verstraelen, M. Waroquier, J. Chem. Phys. 126 (2007) 224102.
[58] A. Ghysels, V. Van Speybroeck, T. Verstraelen, D. Van Neck, M. Waroquier, J. Chem. Theory Comput. 4 (2008) 614.
[59] A. Ghysels, V. Van Speybroeck, E. Pauwels, S. Catak, B.R. Brooks, D. Van Neck, M. Waroquier, J. Comput. Chem. 31 (2010) 994.
[60] B.A. De Moor, A. Ghysels, M.-F. Reyniers, V. Van Speybroeck, M. Waroquier, G.B. Marin, J. Chem. Theory Comput. 7 (2011) 1090.
[61] CMM code, – http://molmod.ugent.be/code/wiki.
[62] T. Verstraelen, V. Van Speybroeck, M. Waroquier, J. Chem. Inf. Model. 48 (2008) 1530.
[63] M.J. Frisch, G.W. Trucks, H.B. Schlegel, G.E. Scuseria, M.A. Robb, J.R. Cheeseman, J.A. Montgomery, T. Vreven, K.N. Kudin, J.C. Burant, J.M. Millam, S.S. Iyengar, J. Tomasi, V. Barone, B. Mennucci, M. Cossi, G. Scalmani, N. Rega, G.A. Petersson, H. Nakatsuji, M. Hada, M. Ehara, K. Toyota, R. Fukuda, J. Hasegawa, M. Ishida, T. Nakajima, Y. Honda, O. Kitao, H. Nakai, M. Klene, X.J.E. Li Jr., Gaussian 03 Revision C. 02 , Gaussian, Inc., Wallingford, CT, 2004.
[64] F. Neese Orca, Version 2.6, An Ab Initio, DFT and Semiempirical Electronic Structure Package , University of Bonn, Germany, 2008.
[65] S. Grimme, J. Comput. Chem. 25 (2004) 1463.
[66] Gaussview 4.1.2, Gaussian, Inc., Wallingford, CT, 2004.
[67] J.P. Merrick, D. Moran, L. Radom, J. Phys. Chem. A 111 (2007) 11683.
[68] K. Hemelsoet, A. Nollet, M. Vandichel, D. Lesthaeghe, V. Van Speybroeck, M. Waroquier, ChemCatChem 1 (2009) 373.
[69] M. Vandichel, D. Lesthaeghe, J. Van der Mynsbrugge, M. Waroquier, V. Van Speybroeck, J. Catal. 271 (2010) 67.
[70] A. Ghysels, D. Van Neck, B.R. Brooks, V. Van Speybroeck, M. Waroquier, J. Chem. Phys. 130 (2009) 084107.
[71] A. Ghysels, V. Van Speybroeck, E. Pauwels, D. Van Neck, B.R. Brooks, M. Waroquier, J. Chem. Theory Comput. 5 (2009) 1203.
[72] A. Ghysels, T. Verstraelen, K. Hemelsoet, M. Waroquier, V. Van Speybroeck, J. Chem. Inf. Model. 50 (2010) 1736.
[73] L. Aramburo-Corrales, B.M. Weckhuysen, in preparation.
[74] K.I. Zamaraev, J.M. Thomas, Adv. Catal. 41 (1996) 335.
[75] C.P. Bezoukhanova, Y.A. Kalvachev, Catal. Rev. Sci. Eng. 36 (1994) 125.
[76] J. Kotrla, L. Nachtigallová, L. Kubelková, L. Heeribout, C. Doremieux-Morin, J. Fraissard, J. Phys. Chem. B 102 (1998) 2454.
[77] S.G. Izmailova, I.V. Karetina, S. Khvoshchev, M.A. Shubaeva, J. Colloids Interface Sci. 165 (1994) 318.
[78] G. Mirth, J.A. Lercher, M.W. Anderson, J. Kinowski, J. Chem. Soc. Faraday Trans. 86 (1990) 3039.
[79] L. Kubelková, J. Nováková, K. Nedomová, J. Catal. 124 (1990) 441.
[80] M.T. Aronson, R.J. Gorte, W.E. Farneth, J. Catal. 98 (1986) 434.
[81] M.T. Aronson, R.J. Gorte, W.E. Farneth, J. Catal. 105 (1987) 455.
[82] R.A. van Santen, G.J. Kramer, Chem. Rev. 95 (1995) 637.
[83] R.A. van Santen, Catal. Today 38 (1997) 377.
[84] J. Sauer, P. Uglieno, E. Garonne, V.R. Saunders, Chem. Rev. 94 (1994) 2095.

[85] F. Haase, J. Sauer, J. Am. Chem. Soc. 117 (1995) 3780.
[86] S.R. Blaszkowski, R.A. van Santen, J. Phys. Chem. 99 (1995) 11728.
[87] J.D. Gale, C.R.A. Catlow, J.R. Carruthers, Chem. Phys. Lett. 216 (1993) 155.
[88] R. Shah, M.C. Payne, M.H. Lee, J.D. Gale, Science 271 (1996) 1395.
[89] R. Shah, J.D. Gale, M.C. Payne, J. Phys. Chem. 100 (1996) 11688.
[90] J.D. Gale, R. Shah, M.C. Payne, I. Stich, K. Terakura, Catal. Today 50 (1999) 525.
[91] F. Haase, J. Sauer, J. Hutter, Chem. Phys. Lett. 266 (1997) 397.
[92] I. Stich, J.D. Gale, K. Terakura, M.C. Payne, Chem. Phys. Lett. 283 (1998) 402.
[93] V.V. Mihaleva, R.A. van Santen, A.P.J. Jansen, J. Phys. Chem. B 105 (2001) 6874.
[94] C. Lo, B.L. Trout, J. Catal. 227 (2004) 77.
[95] R. Shah, J.D. Gale, M.C. Payne, Chem. Commun. (1997) 131.
[96] L.H. Kang, T. Zhang, Z.M. Liu, K.L. Han, J. Phys. Chem. C 112 (2008) 5526.
[97] C.C. Lee, R.J. Gorte, W.E. Farneth, J. Phys. Chem. B 101 (1997) 3811.
[98] C.M. Nguyen, M.F. Reyniers, G.B. Marin, PhysChemChemPhys 12 (2010) 9481.
[99] H. Stach, U. Lohse, H. Thamm, W. Schirmer, Zeolites 6 (1986) 74.
[100] R.E. Richards, L.V.C. Reed, Langmuir 3 (1987) 335.
[101] H.B. Abdul-Rehman, M.A. Hasanain, K.F. Loughlin, Ind. Eng. Chem. Res. 29 (1990) 1525.
[102] J.R. Hufton, R.P. Danner, AIChE J. 39 (1993) 954.
[103] M.S. Sun, O. Talu, D.B. Shah, J. Phys. Chem. 100 (1996) 17276.
[104] F. Eder, J.A. Lercher, J. Phys. Chem. B 101 (1997) 1273.
[105] F.S.M. Eder, J.A. Lercher, J. Phys. Chem. B 101 (1997) 5414.
[106] F. Eder, J.A. Lercher, Zeolites 18 (1997) 75.
[107] J.F. Denayer, G.V. Baron, J.A. Martens, P.A. Jacobs, J. Phys. Chem. B 102 (1998) 3077.
[108] L. Smith, A.K. Cheetham, L. Marchese, J.M. Thomas, P.A. Wright, J. Chen, E. Gianotti, Catal. Lett. 41 (1996) 13.
[109] Y. Jeanvoine, J.G. Angyán, G. Kresse, J. Hafner, J. Phys. Chem. B 102 (1998) 5573.
[110] G.A.V. Martins, G. Berlier, S. Coluccia, H.O. Pastore, G.B. Superti, G. Gatti, L. Marchese, J. Phys. Chem. C 111 (2007) 330.
[111] G.V.A. Martins, G. Berlier, C. Bisio, S. Coluccia, H.O. Pastore, L. Marchese, J. Phys. Chem. C 112 (2008) 7193.
[112] A. Zecchina, G. Spoto, S. Bordiga, PhysChemChemPhys 7 (2005) 1627.
[113] C. Morterra, G. Magnacca, Catal. Today 27 (1996) 497.
[114] S. Bordiga, B. Civalleri, G. Spoto, C. Paze, C. Lamberti, P. Ugliengo, A. Zecchina, J. Chem. Soc. -Far. Trans. 93 (1997) 3893.
[115] V.V. Mihaleva, R.A. van Santen, A.P.J. Jansen, J. Chem. Phys. 120 (2004) 9212.
[116] D. Lesthaeghe, V. Van Speybroeck, M. Waroquier, PhysChemChemPhys 11 (2009) 5222.
[117] A. Zecchina, S. Bordiga, G. Spoto, D. Scarano, G. Spano, F. Geobaldo, J. Chem. Soc. Faraday Trans. 92 (1996) 4863.
[118] M. Rozwadowski, M. Lezanska, J. Wloch, K. Erdmann, R. Golembiewski, J. Kornatowski, Chem. Mater. 13 (2001) 1609.
[119] H.G. Karge, W. Niessen, H. Bludau, Appl. Catal. A 146 (1996) 339.
[120] D. Meloni, D. Martin, P. Ayrault, M. Guisnet, Catal. Lett. 71 (2001) 213.